Reprinted from

NUCLEAR INSTRUMENTS & METHODS IN PHYSICS RESEARCH
Section A

Nuclear Instruments and Methods in Physics Research A 390 (1997) 191–197

Experimental studies on the angular distribution of scintillation light from small BGO crystals

Gerhard M. Haak[a], Nelson L. Christensen[b,*], Bruce E. Hammer[c]

[a]*Department of Electrical and Electronic Engineering, University of Auckland*
[b]*Department of Physics, University of Auckland, Private Bag 92019, Auckland, New Zealand*
[c]*Department of Radiology, University of Minnesota, Minneapolis, MN, USA*

Received 30 July 1996

ELSEVIER

ray-tracing techniques to estimate the coupling efficiency of relevant optics and fibres [16]. Consequently, we used Monte–Carlo simulations and experimental measurements to estimate the characteristics of light emanating from a small, individual scintillation crystal.

Due to the extremely dim nature of the light emitted from a small BGO scintillation crystal, determination of the angular distribution of the light with conventional methods [17] is difficult. We estimate the angular distribution from the intensity profile of the source when projected directly onto a CCD photodetector. Knowledge of the angular distribution of light from scintillation crystals is typically unnecessary, for in most applications the crystals are in direct contact with photodetectors. The irradiance of a crystal has been rarely measured [17]. Fibre–optic coupling of scintillation light is now an important application in the construction of a high-resolution PET ring within an MRI magnet bore [13,14]. Fibre–optic transmission of scintillation light may also prove useful in high-resolution gamma-ray detectors operating in space-constrained or hostile environments, such as particle detectors at accelerators or in a satellite gamma-ray observatory.

2. Computer simulations

To maximise detector resolution, scintillation crystal width should be minimised and we chose to investigate a crystal with $2 \times 2 \times 20$ mm geometry, giving an intrinsic resolution of 1.4 mm, assuming a 1 mm contribution from positron range and non-colinearity effects. The 1 mm contribution was estimated from the slight reduction in point-spread function for a ^{18}F source due to the magnetic field [2]. Using a crystal with a larger transverse width will nullify the advantages gained from the use of the high magnetic fields, whilst a smaller crystal reduces the light output without a substantial increase in resolution.

The refractive index and surface properties of a crystal define its physical characteristics, i.e. polished with no external reflector, or polished and treated with a diffuse Lambertian reflector. A Lambertian reflector or perfectly diffuse radiating surface has the amount of light leaving that surface proportional to $\cos\theta$, where angle θ is between the normal of the elemental area of the surface and the direction of light propagation. Light collection was taken from a clear face. We did not consider the use of specular reflectors because they typically have low reflectivities, thus adversely affecting light output [18]. In the computer model, we vary the external reflector's reflectivity between 0 and 1. The optical attenuation length of the scintillation light was also a variable. The attenuation length is defined as the distance over which the light intensity decreases by 1/e. As the attenuation length has little effect on the final light output from the crystal [18], this was kept constant at 1 m for all simulations.

3. Angular distribution

3.1. Experiments

A $2 \times 2 \times 20$ mm BGO crystal is polished on all sides and a single 2×2 mm face is roughened with small-grit silicon carbide paper until the surface appears cloudy. To emulate a diffuse reflector, this surface is treated with TiO_2 paint, approximately 0.5 mm thick, to ensure that maximum light is reflected, and not transmitted through the deposition. The crystal is mounted on an aluminium positioning platform (Fig. 1) with the clear face facing

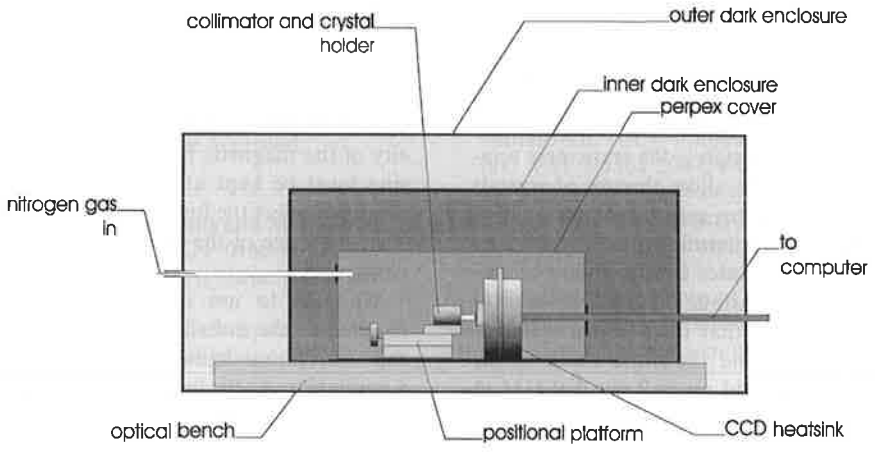

Fig. 1. Experimental apparatus used for the measurement of the illuminance function of the BGO crystal. The CCD operated in a nitrogen atmosphere to prevent misting of the CCD face when operated at -25 ± 0.1°C. Only the CCD was cooled. The crystal remained at ambient temperature, nominally between 17°C and 20°C.

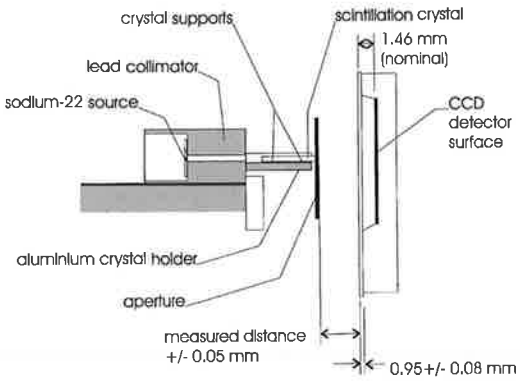

Fig. 2. Blown-up cross-sectional view of source collimator and crystal holder. A 2×2 mm aperture was used to prevent light emitted from the side of the crystal being detected by the CCD. In the analysis, the CCD coverglass is assumed to be 0.95 mm thick, 1.46 mm from the top of the glass to the detector surface.

a Texas Instruments high blue response TC241 754×244-pixel CCD image sensor, 8.8 mm wide, 6.6 mm high, operating at -25°C in a nitrogen atmosphere and housed within a light-tight enclosure. The distance from the top of the CCD coverglass to the image sensor is typically 1.46 mm (Fig. 2). The glass is 0.95 ± 0.08 mm thick and has an index of 1.53 [19]. The crystal remains at ambient room temperature, nominally between 17°C and 20°C, and rests on two small 3×1 mm polished aluminium supports to ensure that the specularity of the polished surfaces is not disturbed by contact with the crystal holder (Fig. 2).

The crystal face is parallel to the CCD and successive exposures at 0.46 ± 0.05 mm, 0.91 ± 0.05 mm, 1.37 ± 0.05 mm and 1.82 ± 0.05 mm from the CCD coverglass of 2 min duration are taken of the crystal. A ^{22}Na source (1-μCi point-source) provided gamma-rays at 511 and 1275 keV. The image is read out as a 250 wide by 120 high pixel image. A saved dark image, taken in identical conditions but without the BGO and radioactive source removed, is subtracted from each exposure to remove background noise effects. Using a pixel brightness histogram, the maximum pixel intensity is determined for intensity range determination. Each pixel is 34.4 μm wide and 54.0 μm high. Based on this information, the image is saved in 8 bit monochrome PC TIFF format. The images are converted into 85×64 bit-mapped monochrome images, where each pixel is 100 μm high and 100 μm wide, thus improving the signal-to-noise ratio. All image conversion and processing methods are linear transformations, and pixel brightness at all stages is a linear function of photon count.

3.2. Theoretical images

The angular distribution of rays emanating from an incoherent planar light source is typically expressed as a function of the angle of emission [20]:

$$\frac{\partial P(\omega)}{\partial \omega \, \partial \Omega} = K \cos^n(\omega), \tag{1}$$

where P is the power, ω is the angle of emission, Ω is the solid angle of measurement, K is a proportionality factor and n is the directivity exponent. The solid angle decomposes into a sine factor, i.e.

$$\frac{\mathrm{d}P(\omega)}{\mathrm{d}\omega} = K \sin(\omega)\cos^n(\omega). \tag{2}$$

The simulations for the case, where a $2 \times 2 \times 20$ mm crystal has a diffuse Lambertian reflector painted on the back of the crystal, produces an angular distribution as shown in Fig. 3. In the same figure, the angular distributions that are expected for incoherent sources with n ranging from 0.5 to 1.5 are indicated. As can be seen, the angular distribution from the crystal can be described by a function with n between 1 and 1.5, peaking at approximately 42°. Sources with $n = 1$ and 1.5, peak at 45° and 39°, respectively. To estimate n for the experimental intensity plots, theoretical intensity plots for $n = 0$–3, are directly compared with the experimental image.

For a given point source, the power is projected directly onto a detector surface as shown in Fig. 4. The area of the circle on the detector surface is

$$A = \pi R^2 = \pi f(\omega)^2, \tag{3}$$

where R is a function of ω, D_1, D_2 and D_3. In the experimental measurements, distances D_{1-3} are treated as constants and the irradiance on the scribed circle at angle ω is consequently equal to

$$\frac{\mathrm{d}P(\omega)}{\mathrm{d}A} = \frac{\mathrm{d}\omega}{\mathrm{d}A}\frac{\mathrm{d}P(\omega)}{\mathrm{d}\omega} = \frac{K \sin(\omega)\cos^n(\omega)}{2\pi f(\omega) f'(\omega)}. \tag{4}$$

Due to the coverglass between the sensor surface and source, for our experimental case,

$$R = f(\omega) = (D_1 + D_3 - D_2)\tan(\omega) + D_2 \tan\left(\arcsin\left[\frac{n_1}{n_2}\sin\omega\right]\right), \tag{5}$$

where the variables are as defined in Fig. 4. Eqs. (4) and (5) yield a theoretical point-spread-function that is calculated and convolved with the 2×2 mm crystal source face. As the simulations indicate the source to be uniformly bright across the face, a uniformly bright source is used for the theoretical images.

3.3. Fitting and comparison

Consider an experimental image E^{x} and calculated image E^{d}. Let the pixel intensities E^{d}_{ij} be defined as

$$E^{\mathrm{d}}_{ij} = g(i,j), \tag{6}$$

and E^{x}_{ij} as

$$E^{\mathrm{x}}_{ij} = \lambda g(i,j) + \delta(i,j) + k, \tag{7}$$

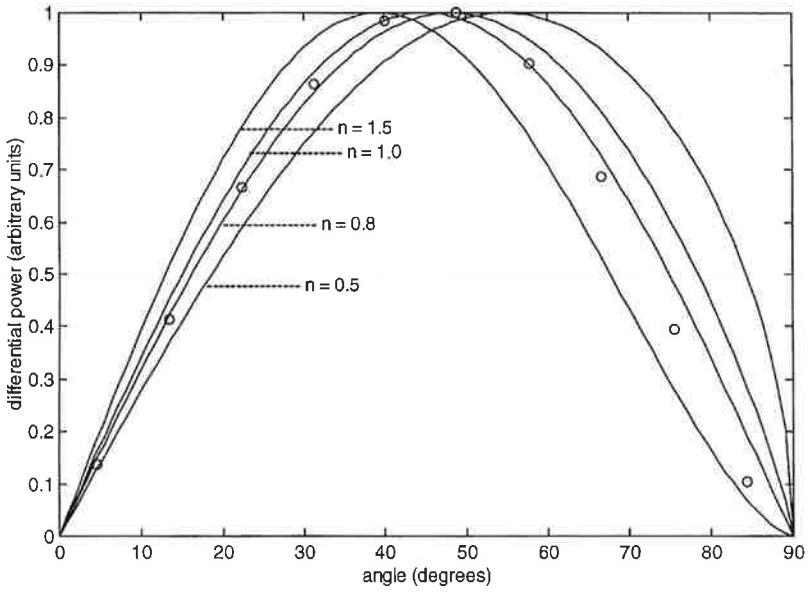

Fig. 3. Angular distributions of light emitted from incoherent Lambertian sources for $n = 0.5$, 0.8, 1.0 and 1.5 (indicated), where n is the exponent of directivity. Also shown (○) is the simulated angular distribution expected from a small BGO crystal of dimensions $2 \times 2 \times 20$ mm, with 5 surfaces polished and the back 2×2 mm roughened and covered with a diffuse Lambertian reflector.

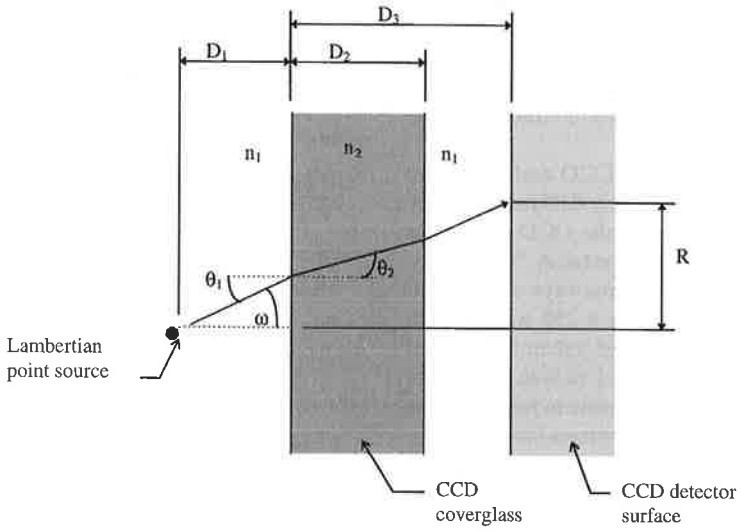

Fig. 4. Measurements used to derive Eq. 5. D_1 is the measured distance, D_2 and D_3 are given by the manufacturer (Fig. 2). Also, n_1 is the optical index of refraction in vacuum (1), and n_2 is the optical index of the CCD coverglass (1.53).

where λ is a mean linear scaling factor, $\delta(i,j)$ is a noise factor dependent on the sensitivity variation of the CCD elements and Poisson nature of the signal (and has a mean of 0), and k is the mean dark-current component, assumed constant across the CCD. $\lambda g(i,j)$ is the actual intensity without noise components. If the two images are identical and assuming $\delta(i,j) = 0$ for all i and j then,

$$E_{ij}^{\mathrm{d}} = \frac{1}{\lambda} E_{ij}^{\mathrm{x}} - \frac{k}{\lambda} = \frac{1}{\lambda} E_{ij}^{\mathrm{x}} - \beta. \tag{8}$$

Thus, setting

$$I_{ij} = \frac{1}{\lambda} E_{ij}^{\mathrm{x}} - \beta, \tag{9}$$

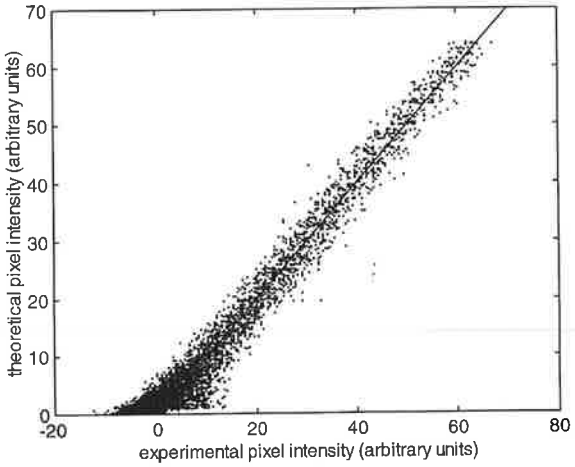

Fig. 5. Plot of $g(i,j)$ against $I(i,j)$ for $\lambda = 0.80$, $\beta = 12.45$ and $n = 0.8$. For the least-square analysis, pixel intensities below the FWHM of the measured image were cut due to high noise at lower intensities. The solid line represents the ideal case, with no noise.

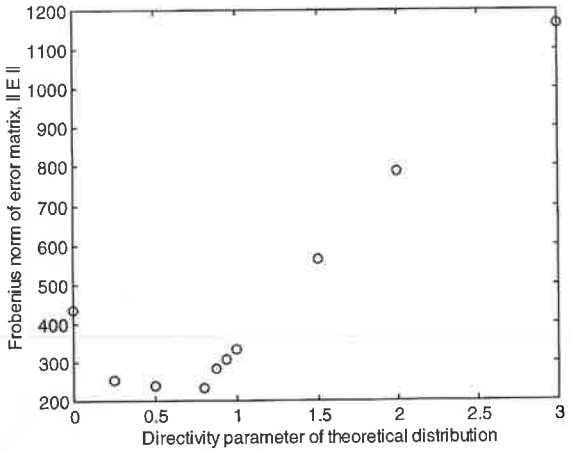

Fig. 6. Frobenius matrix norm of the error matrix E^{error} for $n = 0$–3.

and a plot of E^{d}_{ij} versus I_{ij}, where i and j are the pixel locations, will reveal a linear relationship with a slope of 45° for a given λ and β. The difference (or error) between the two images is

$$E^{\text{error}}_{ij} = E^{\text{d}}_{ij} - \left(\frac{1}{\lambda}E^{\text{x}}_{ij} - \beta\right) = \frac{1}{\lambda}\delta(i,j) \tag{10}$$

an $(i \times j)$ matrix. A scalar measure of the deviation between the two images is the Frobenius matrix norm of E^{error}, $\|E^{\text{error}}\|$. The constants λ and β are found through a least-squares deviation analysis of a plot of E^{d}_{ij} against E^{x}_{ij}. For the least-squares analysis, pixel intensities below the FWHM of the experimental data (and correspondingly, the theoretical image) are cut to reduce unnecessary weighting on the noise floor. This technique is similar to that used to fit multimode fibre–optic intensity profiles [21].

The result of the fitting procedure is shown in Figs. 5–8. A plot of $g(i,j)$ against $I(i,j)$ is given in Fig. 5 at 0.046 ± 0.05 mm from the CCD for $n = 0.8$, and the ideal case is illustrated on the same graph with a 45° line. The

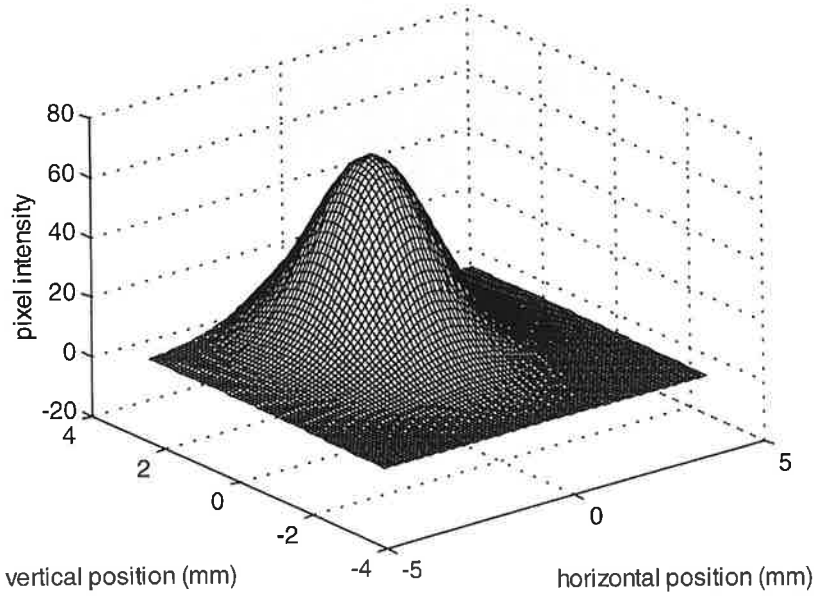

Fig. 7. Calculated image, $g(i,j)$, at 0.46 ± 0.05 mm from the CCD coverglass for $n = 0.8$.

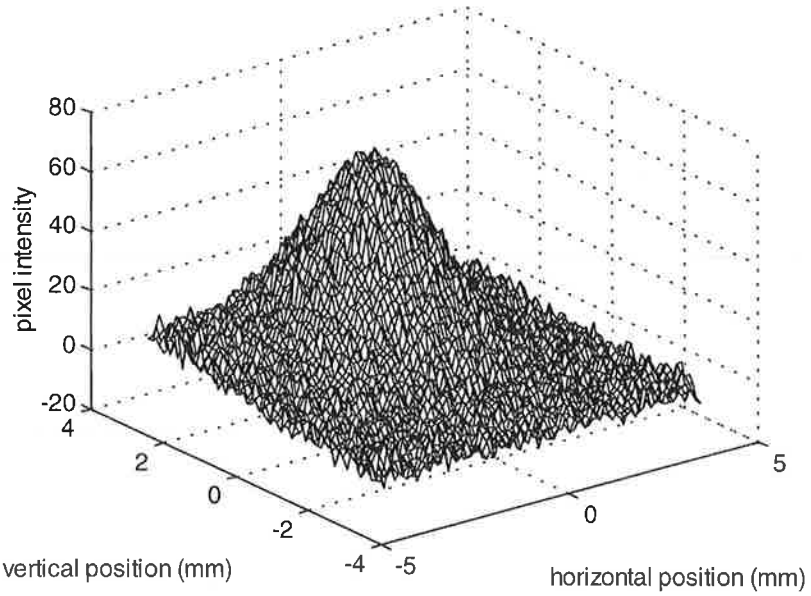

Fig. 8. Measured image, $I(i,j)$, at 0.46 ± 0.05 mm from the CCD coverglass for $\lambda = 0.80$ and $\beta = 12.45$.

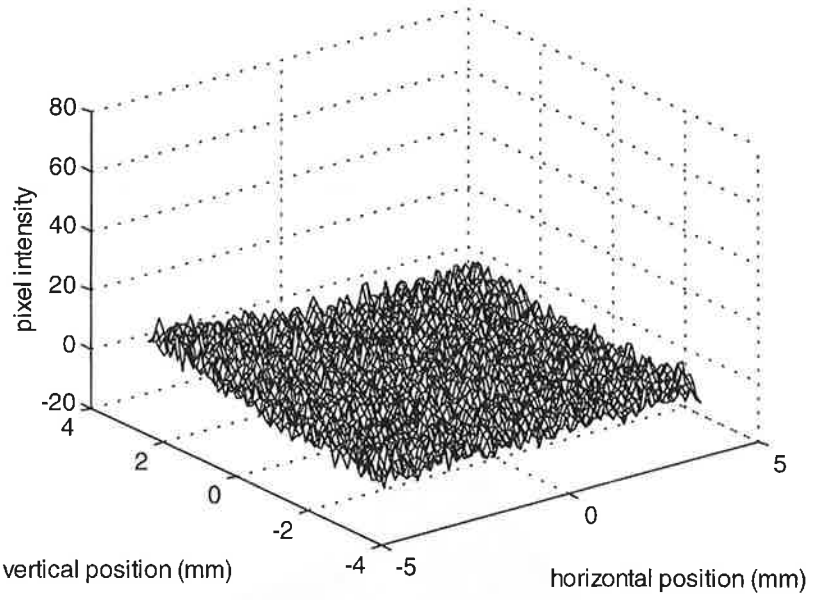

Fig. 9. Calculated image subtracted from the measured image (λ and β as given previously), revealing the noise $(1/\lambda)\delta(i,j)$.

lowest value for $\|E^{\text{error}}\|$ is found to be for $n \approx 0.8$, with $\lambda = 0.80$ and $\beta = 12.45$. Fig. 6 shows $\|E^{\text{error}}\|$ for case comparisons, where $n = 0$–3, and provides an approximate guide to the magnitude of deviation for these values. A similar analysis for the data when the crystal face was 0.91 mm from the CCD coverglass gave an optimal Lambertian index of $n \approx 1.0$, while for 1.37, it was $n \approx 0.8$. When the distance was 1.82 mm, the light intensity was too low for any determination of n. The final result is more clearly conferred by Figs. 7–9. Fig. 7 is the calculated form of the image for a source (at a distance 0.46 mm) after convolution with a PSF determined from a Lambertian point source with $n = 0.8$. The experimental image is shown in Fig. 8. After subtraction of the ideal image from the experimental image, the noise remains (Fig. 9).

4. Discussion

The development of an efficient and spatially compact means to detect scintillator-produced light within the inhospitable environment of an MRI magnet is essential for the development of a dual PET–MRI scanner [12–14]. The use of fibre–optics to transport scintillation light to photodetectors meters away is a likely and promising technique [13,14]. Knowledge of the angular distribution of light produced by the scintillation crystals is crucial for the design and implementation of a hybrid PET–MRI scanner.

Our Monte–Carlo studies indicate that the $2 \times 2 \times 20$ mm BGO crystal behaves as a Lambertian source of index $n \approx 1$. The experimental results presented in this paper agree with this conclusion. Given the above analysis, it is now possible to use the extensive work published on the coupling of LEDs into optical fibre to perform a thorough analysis of the possible coupling methods that may be applied in a future PET–MRI device [21].

Acknowledgements

This work was supported by grants from the Auckland Medical Research Foundation, Health Research Council of New Zealand, University of Auckland Research Committee and the National Institutes of Health (NIH/1R29-CA65523-01A1). We would also like to thank Dr. Jack Storey for the use of the astronomical CCD camera.

References

[1] M.M. Ter-Pogossian, J. Nucl. Med. 26 (1985) 1487.
[2] R.R. Raylman, B.E. Hammer, N.L. Christensen, IEEE Trans. Nucl. Sci. 43 (1996) 2406.
[3] T.F. Budinger, S.E. Derenzo, R.H. Huseman, W.J. Jaguest, P.E. Valk, Acta Radiol. 376 (1991) 15.
[4] Daniel W. Rickey, Richard Gordon, Walter Huda, Automedica 14 (1992) 355.
[5] H. Iida, I. Kanno, S. Miura, M. Murakami, K. Takahashi, K. Uemura, IEEE Trans. Nucl. Sci. NS-33 (1986) 597.
[6] B.E. Hammer, N.L. Christensen, IEEE Trans. Nucl. Sci. NS-42 (1995) 1371.
[7] B.E. Hammer, N.L. Christensen, B. Heil, Med. Phys. 21 (1994) 1917.
[8] William W. Moses, Stephen E. Derenzo, Thomas F. Budinger, Nucl. Instr. and Meth. A 353 (1994) 189.
[9] Simon R. Cherry, Yiping Shao, Martin P. Tornai, Stefan Siegel, Anthony R. Ricci, Michael E. Phelps, IEEE Trans. Nucl. Sci. NS-42 (1995) 1058.
[10] C. Schmelz, S.M. Bradbury, I. Holl, E. Lorenz, D. Renker, S. Ziegler, IEEE Trans. Nucl. Sci. NS-42 (1995) 1080.
[11] B. Hammer, U.S. Patent #4,939,464 (1990).
[12] B.E. Hammer, Physica Medica/Giardini editori e Stampatori, Pisa, Italy. vol. XII Suppl. 1, May 1996. Proc. ESI Seminar: Medical Imaging and New Types of Detectors, Archamps, France, May 20–24, 1995.
[13] G.M. Haak, N.L. Christensen, B.E. Hammer, IEEE Trans. Nucl. Sci., (1996), submitted.
[14] Y. Shao, S.R. Cherry, S. Siegel, R.W. Silverman, P.K. Marsden, Proc. 43rd Ann. Meeting of the Society of Nuclear Medicine, vol. 37, 5, 1996, p. 85.
[15] A. Nicia, Appl. Opt. 20 (1981) 3136.
[16] Allan W. Snyder, D.J. Mitchell, J. Opt. Soc. Amer. 64 (1974) 599.
[17] M.J. Kim, J.C. Dainty, A.T. Friberg, A.J. Sant, J. Opt. Soc. Amer. A 7 (1990) 569.
[18] M.A. Mosleh-Shizazi, W. Swindell, P.M. Evans, Nucl. Instr. and Meth. A 348 (1994) 563.
[19] Texas Instruments, Area Array Image Sensor Products Data Manual, 1993, pp. 2–135.
[20] Helmut F. Wolf, Handbook of Fibre Optics Theory and Application, Garland Publishing, Inc, 1979, p. 139.
[21] G. He, F.W. Cuomo, J. Lightwave Technol. 9 (1991) 545.